

## Article

# Interface Engineering of SRu-mC<sub>3</sub>N<sub>4</sub> Heterostructures for Enhanced Electrochemical Hydrazine Oxidation Reactions

Ajay Munde <sup>1,†</sup>, Priti Sharma <sup>2,†</sup>, Somnath Dhawale <sup>1</sup> , Ravishankar G. Kadam <sup>2</sup>, Subodh Kumar <sup>3</sup> , Hanumant B. Kale <sup>4</sup> , Jan Filip <sup>2</sup>, Radek Zboril <sup>2,5</sup>, Bhaskar R. Sathe <sup>1,\*</sup>  and Manoj B. Gawande <sup>2,4,\*</sup> 

<sup>1</sup> Department of Chemistry, Dr. Babasaheb Ambedkar Marathwada University, Aurangabad 431004, Maharashtra, India

<sup>2</sup> Regional Centre of Advanced Technologies and Materials, Czech Advanced Technology and Research Institute, Palacký University, Šlechtitelů 27, 779 00 Olomouc, Czech Republic

<sup>3</sup> Department of Inorganic Chemistry, Faculty of Science, Palacký University, 17. Listopadu 12, 771 46 Olomouc, Czech Republic

<sup>4</sup> Department of Industrial and Engineering Chemistry, Institute of Chemical Technology, Mumbai-Marathwada Campus, Jalna 431213, Maharashtra, India

<sup>5</sup> CEET, Nanotechnology Centre, VŠB-Technical University of Ostrava, 17. Listopadu 2172/15, 708 00 Ostrava, Czech Republic

\* Correspondence: bsathe.chemistry@bamu.ac.in (B.R.S.); mb.gawande@marj.ictmumbai.edu.in (M.B.G.)

† These authors contributed equally to this work.



**Citation:** Munde, A.; Sharma, P.; Dhawale, S.; Kadam, R.G.; Kumar, S.; Kale, H.B.; Filip, J.; Zboril, R.; Sathe, B.R.; Gawande, M.B. Interface Engineering of SRu-mC<sub>3</sub>N<sub>4</sub> Heterostructures for Enhanced Electrochemical Hydrazine Oxidation Reactions. *Catalysts* **2022**, *12*, 1560. <https://doi.org/10.3390/catal12121560>

Academic Editors: Keith Hohn, Kotohiro Nomura, Evangelos Topakas, Vincenzo Baglio, C. Heath Turner, Leonarda Liotta, Jean-François Lamonier and Maria A. Goula

Received: 14 October 2022

Accepted: 21 November 2022

Published: 2 December 2022

**Publisher's Note:** MDPI stays neutral with regard to jurisdictional claims in published maps and institutional affiliations.



**Copyright:** © 2022 by the authors. Licensee MDPI, Basel, Switzerland. This article is an open access article distributed under the terms and conditions of the Creative Commons Attribution (CC BY) license (<https://creativecommons.org/licenses/by/4.0/>).

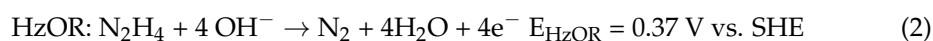
**Abstract:** Hydrazine oxidation in single-atom catalysts (SACs) could exploit the efficiency of metal atom utilization, which is a substitution for noble metal-based electrolyzers that results in reduced overall cost. A well-established ruthenium single atom over mesoporous carbon nitride (SRu-mC<sub>3</sub>N<sub>4</sub>) catalyst is explored for the electro-oxidation of hydrazine as one of the model reactions for direct fuel cell reactions. The electrochemical activity observed with linear sweep voltammetry (LSV) confirmed that SRu-mC<sub>3</sub>N<sub>4</sub> shows an ultra-low onset potential of 0.88 V vs. RHE, and with a current density of 10 mA/cm<sup>2</sup> the observed potential was 1.19 V vs. RHE, compared with mesoporous carbon nitride (mC<sub>3</sub>N<sub>4</sub>) (1.77 V vs. RHE). Electrochemical impedance spectroscopy (EIS) and chronoamperometry (i-t) studies on SRu-mC<sub>3</sub>N<sub>4</sub> show a smaller charge-transfer resistance (R<sub>ct</sub>) of 2950 Ω and long-term potential, as well as current stability of 50 h and 20 mA/cm<sup>2</sup>, respectively. Herein, an efficient and enhanced activity toward HzOR was demonstrated on SRu-mC<sub>3</sub>N<sub>4</sub> from its synergistic platform over highly porous C<sub>3</sub>N<sub>4</sub>, possessing large and independent active sites, and improving the subsequent large-scale reaction.

**Keywords:** single-atom catalysts; mesoporous carbon nitride; nanoelectrodes; hydrazine oxidation reactions

## 1. Introduction

For developed countries, revolution necessitates growth in energy crises. Regularly, and regrettably, the excessive use of fossil energy resources based on hydrocarbons (petrol, diesel, and coal) results in permanent environmental issues [1,2]. This is mostly owing to their usage in transportation, industrialization, improvements in living standards, and a variety of other human-based carbon footprint activities [3]. More importantly, environmental issues are related to the use of carbon-based energy sources, owing to growth in a large number of greenhouse gases, such as CO<sub>2</sub> and other pollutants, including oxides of nitrogen and sulfur, i.e., (NO)<sub>x</sub> and (SO)<sub>x</sub> which have major environmental and health consequences [3,4]. To address these challenges, researchers worldwide are developing clean fuel techniques for producing clean and energy-efficient fuels, such as H<sub>2</sub> from water, and bio-agricultural waste, including alcohols and ammonia/hydrazine [5–8]. A cost-effective and long-term approach for the simultaneous development of H<sub>2</sub> and O<sub>2</sub> produced through electrochemical H<sub>2</sub>O splitting processes has recently been developed [8–10]. In order to

break the O-H bond and produce molecular O<sub>2</sub>, the electrochemical H<sub>2</sub>O oxidation process requires a more complicated reaction. This reaction is sluggish and requires huge potential; therefore, it is desirable to replace the OER with a more oxidizable (at a lower potential) anodic reaction built on lower-molecular-weight organic molecules to generate H<sub>2</sub> at a lower potential (0.37 V vs. SHE) from the oxidation of species such as methanol, ethanol, urea, furfural, and hydrazine (equations 1 and 2) [7,11–17]. Direct hydrazine fuel cells (DHFCs) are potential power devices, attractive for their simple storage and transportation of liquid hydrazine fuel, low theoretical cell voltage, lack of CO<sub>2</sub> gas emissions, and low risk of CO poisoning [18]. Hydrazine is the simplest inorganic compound and is well known for its highly reactive base nature and utility as a reducing agent via electron donation. Such unique features make hydrazine an ideal compound for use as a fuel in direct fuel cells as a source of H<sub>2</sub> [19,20]. Substituted anodic reactions, such as hydrazine oxidation, may be another effective and beneficial way to decrease total electrolysis voltage, inspired by hydrazine fuel cells and the processes of chloro-alkali industries [21]. As a result, the substituted anodic hydrazine oxidation might minimize the overall cost and over potential of the entire electrolysis cell with the use of an efficient electrocatalyst, allowing for the generation of pure H<sub>2</sub> with lower power. Moreover, the process has other advantages, such as the breakdown into harmless compounds such as N<sub>2</sub> and H<sub>2</sub>O [22].



Recently, Chen and co-workers demonstrated the application of RhP ultrathin nanosheets for the enhanced electro-oxidation of hydrazine, and tested the impact of phosphorus on the electronic structures of Rh atoms in RhP [19]. Muthukumar et al. reported that the synthesis of Au-cit nanoparticles immobilized on Co(II)MTpAP shows superior catalytic activity towards hydrazine oxidation, compared with Co(II) complexes without Au NPs. These results were attributed to the synergistic effect arising from both Au NPs and Co(II) complexes [23]. Ji and co-workers proposed Co- and N-doped nonporous carbon (Co-NPC NNs), and showed that the higher content of pyridinic N (29.7%) was mainly due to the insertion of Co nanoparticles providing a large active area, and the presence of Co<sup>2+</sup> active catalytic sites promoted hydrazine oxidation [24]. Ding et al. explored a MnO/N-C-based nanocomposite for DHFCs that demonstrated exceptionally high performance due to the synergistic properties of MnO and N-C in the composite [25].

In recent years, single-atom catalysts (SACs) have exclusively enhanced the efficiency of metal atom utilization, achieving extraordinary activity and significantly exceeding comparable nanomaterials in terms of stability and selectivity in electrocatalytic applications [12,26,27]. Recently, some SACs have also been reported to catalyse various electrochemical reactions, including electrocatalytic hydrazine, alcohol oxidation, and CO<sub>2</sub> reduction, with excellent efficiency [28,29]. Therefore, despite the challenges, it is highly desirable to develop a universal approach for the fabrication of SACs that can be applied to a wide range of metals. However, there are also challenges when applying SACs in practical systems for electrocatalytic reactions due to the tendency of single atoms to form clusters and to leach out during interfacial reactions. One effective strategy for addressing these challenges involves the use of 2D materials as a substrate to anchor the single atoms. In recent years, metal-free semiconductor (n-type) polymer-based g-C<sub>3</sub>N<sub>4</sub> has attracted worldwide attention for its unique characteristics such as large surface area, long catalytic durability, low band gap with sp<sup>2</sup> hybridized unique nitrogen, and carbon with π(π)-conjugated systems. However, g-C<sub>3</sub>N<sub>4</sub> has strong covalent bonds which elaborate its extended stability, since it is well synthesized by following simple fabrication methods and using low-cost starting materials, such as urea, dicyanamide, etc. [30,31]. On the other hand, during the synthesis of hybrid materials, metal ions can easily anchor to the cavities. This simultaneously creates a heptazine ring, which alters the properties of the composite. The central aim of metal loading is to achieve higher chemical stability, reflected in the

synergistic effect of the two component metals, and to obtain catalysts with more favourable properties [32]. Recently, *g*-C<sub>3</sub>N<sub>4</sub> has received significant interest as a support material for the manufacture of SACs because of its ability to tune the electronic properties of the guest atoms and further support electron transfer at the electrified interface [33]. Since three different types of N-atoms (pyridinic-N, pyrrolic-N, and graphitic-N) are present in *g*-C<sub>3</sub>N<sub>4</sub> derivatives, it can render strong interactions with single atoms, resulting in the formation of SACs, as well as hindering the aggregation of nanoparticles during catalytic reactions [12,29]. However, for various carbonaceous materials, such as CNT and graphene, nitrogen-based materials have been employed as electrodes for electrochemical storage. Since such materials are cheaper and possess good electronic conductivity and chemical stability, they are readily considered for hydrogen storage technologies [34–36].

In pursuing single-atom research, our research group recently reported an effective strategy for the introduction of single-site Ru atoms into a mesoporous carbon nitride (mC<sub>3</sub>N<sub>4</sub>) network [18]. Furthermore, in the current research, appreciable enhancement in the electrochemical properties of as-synthesized ruthenium single atoms over mesoporous C<sub>3</sub>N<sub>4</sub> (SRu-mC<sub>3</sub>N<sub>4</sub>) has been observed. The formulated SRu-mC<sub>3</sub>N<sub>4</sub> was further applied to the electro-oxidation of hydrazine under various parameters, and these combined studies are explored in detail herein. However, to the best of our knowledge, there are no other reports to be found on SRu-mC<sub>3</sub>N<sub>4</sub> and hydrazine oxidation reactions, and hence these findings will enrich further research in the field of the electro-oxidation of hydrazine.

## 2. Results and Discussion

The physical properties of the synthesized material were evaluated using different morphological and structural characterization tools. Wide-angle XRD measurements displayed a strong peak at 27.4 degrees and a small peak at 13 degrees (see Supplementary Information Figure S1). The observed peaks were attributed to the interlayer spacing of the mesoporous *g*-C<sub>3</sub>N<sub>4</sub> sheets, with the (002) and (100) planes' pronounced peaks representing the graphitic interlayer and the in-plane structural packing motif, respectively. However, the XRD patterns for SRu-mC<sub>3</sub>N<sub>4</sub> exhibited few peaks characteristic of Ru-based nanoparticles [33].

To ascertain the chemical composition of the fabricated material, it was examined using XPS analysis. High-resolution Ru 3d XPS spectrum data exhibit a clear peak pair for Ru3d<sub>5/2</sub> at 280.94 and 282 eV, and the next peak pair at 285.11 and 286.2 eV corresponds to Ru3d<sub>3/2</sub>, simultaneously confirming the presence of two Ru species possessing the different oxidation states Ru<sup>4+</sup> and Ru<sup>2+</sup>, respectively (Figure 1A, and see Supplementary Information Figure S2). Apart from ruthenium, the key element of the synthesized material, such as the N 1s signal band of SRu-mC<sub>3</sub>N<sub>4</sub>, deconvolutes into three characteristics peaks of *g*-C<sub>3</sub>N<sub>4</sub> (pyridinic-N, pyrrolic-N, and graphitic-N). These results clearly support the fact that ruthenium is attached to two different sites. The Raman spectrum results support the existence of characteristic C–N, D, and G bands of synthesized SRu-mC<sub>3</sub>N<sub>4</sub> and graphitic carbon nitride materials. Furthermore, the clearly emerged breadth of bands D and G visualizes the defective structure of the carbon matrix (Figure 1B). In addition, EXAFS and XANES characterization in our previous research established the existence of active sites in SRu-mC<sub>3</sub>N<sub>4</sub> [18].

The representative high-resolution transmission electron microscopy (HR-TEM) image clearly supports the absence of any Ru-based centres over the surface of mC<sub>3</sub>N<sub>4</sub> sheets (Figure 2). Furthermore, the present high-angle annular dark-field scanning transmission electron microscopy (HAADF-STEM) element mapping images disclose the distribution of Ru over the entire mesoporous mC<sub>3</sub>N<sub>4</sub> structure (Figure 2C–G). The Ru single atoms are highlighted in white-dotted circles in the highly magnified HR-TEM image (Figure 2H).

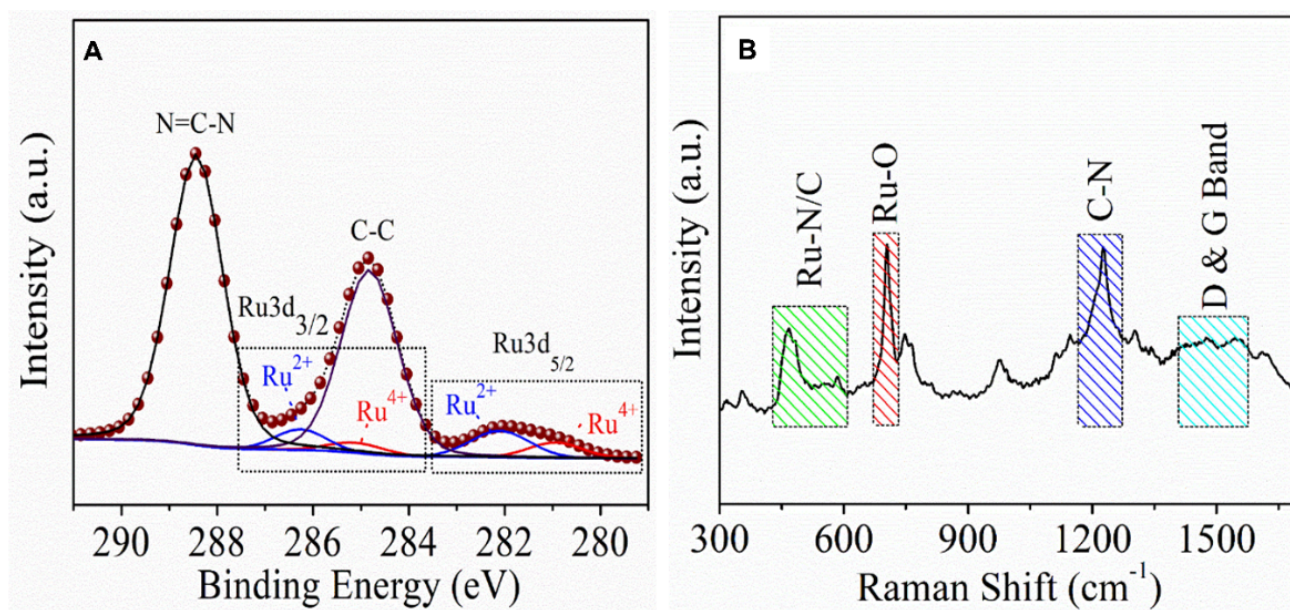


**Figure 1.** (A) Ru 3d high-resolution XPS spectra of SRu-mC<sub>3</sub>N<sub>4</sub>; (B) Raman spectra of SRu-mC<sub>3</sub>N<sub>4</sub>.

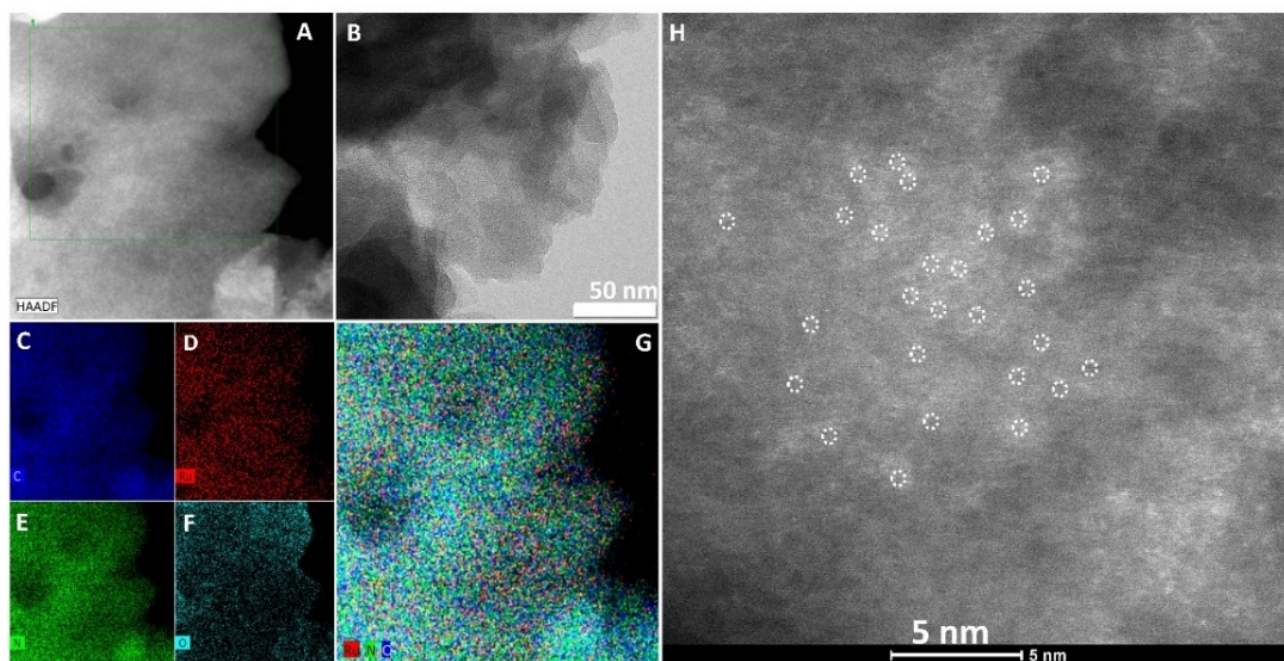


**Figure 2.** HR-TEM analysis of SRu-mC<sub>3</sub>N<sub>4</sub>: (A) HAADF-STEM elemental mapping images showing O, N, Ru, and C individually (C–F) and (G) Ru, N, and C together (scale: 40 nm); (B) TEM image at 50 nm; and (H) HR-TEM image at 5 nm exhibiting the ruthenium single atom existence over mC<sub>3</sub>N<sub>4</sub> support.

### 2.1. Electrochemical and Electrocatalytic Studies

All electrochemical and electrocatalytic studies were performed on a CHI-660E electrochemical workstation (CH-Instrument) with three electrode systems. Modified glassy carbon (GC, 3 mm dia.) was used as the working electrode, and Pt foil and SCE were used as the counter and reference electrodes, respectively, in 0.5 M KOH solution. The GC electrode cleaning was carried out with three different sizes of Al<sub>2</sub>O<sub>3</sub> powder (1, 0.3 and 0.05 μm) followed by rinsing in deionized water and sonication in ethanol for 5 min, in sequence, to remove inorganic and organic impurities, respectively. The preparation of

the working electrode includes calculated amounts, i.e., 5 mg of catalyst dispersed in 1 mL isopropyl alcohol under an ultrasonic bath stirred for 40 min. An aliquot of the slurry was dropped onto the pre-polished GC electrode using a micropipette and dried naturally. The loading of the calculated amount (5  $\mu$ L) of electrocatalyst on the GC electrode was used for the normalization of the electrochemical data with a calculated amount of SRu-mC<sub>3</sub>N<sub>4</sub>. The following equation 3 was used to convert the electrochemical measurements against the reference SCE into the reversible hydrogen electrode (RHE):

$$V_{(\text{RHE})} = V_{\text{SCE}} + 0.2412 + 0.059 \cdot \text{pH} \quad (3)$$

Electrochemical studies on the electro-oxidation of hydrazine on the as-synthesized SRu-mC<sub>3</sub>N<sub>4</sub> nanocomposite have been investigated with a typical three-electrode system, with 6  $\mu$ M N<sub>2</sub>H<sub>4</sub> + 0.5 M KOH electrolyte mixture as a model reaction for direct fuel cells. Accordingly, Figure 3A demonstrates the superimposed LSV for bare GCE, m-C<sub>3</sub>N<sub>4</sub> (ii), and SRu-mC<sub>3</sub>N<sub>4</sub> (iii) in 6  $\mu$ M N<sub>2</sub>H<sub>4</sub> + 0.5 M KOH at a scan rate of 50 mV/s. Moreover, LSV data for bare GCE showed no significant change and confirm the inactivity toward hydrazine, while m-C<sub>3</sub>N<sub>4</sub> showed the onset potential of 1.2 V vs. RHE, and the lower potential of 1.77 V vs. RHE required for the 10 mA/cm<sup>2</sup> current density. More significantly, SRu-mC<sub>3</sub>N<sub>4</sub> showed the ultra-low onset potential of 0.88 V vs. RHE, and a current density of 10 mA/cm<sup>2</sup> was observed at 1.19 V vs. RHE. Moreover, the electrocatalytic performance of SRu-mC<sub>3</sub>N<sub>4</sub> toward hydrazine was tested in a controlled experiment in 0.5 M KOH with and without hydrazine (see Supplementary Information Figure S3), further confirming the response corresponding to hydrazine oxidation. In addition, we investigated the effect of the w/w% loading of Ru on m-C<sub>3</sub>N<sub>4</sub> toward hydrazine oxidation, and showed that SRu-mC<sub>3</sub>N<sub>4</sub> (A1) (1.35 wt.%), SRu-mC<sub>3</sub>N<sub>4</sub> (A2) (2.74 wt.%), and SRu-mC<sub>3</sub>N<sub>4</sub> (A3) (1.86 wt.%) possessed lower electrochemical activity compared with SRu-mC<sub>3</sub>N<sub>4</sub> (0.54 %). This may be due to the loading of an individual identity of a single atom and its altered reactivity to Ru clusters/nanostructures, as shown in Figure 3A. The high electrochemical performance of the SRu-mC<sub>3</sub>N<sub>4</sub> catalyst over individual atoms is thus attributed to the synergistic effect between the single Ru atoms and active N-centres from the mC<sub>3</sub>N<sub>4</sub> nanosheets. The internal formation of Ru-N/C intercalation in the first coordination shell and the attainment of synergy in the N–Ru–N connection may promote electrooxidation of hydrazine. In addition, Figure 3B shows the ultra-low potential of SRu-mC<sub>3</sub>N<sub>4</sub> SACs, even at a comparatively high current density of 10 mA/cm<sup>2</sup>. Additionally, small shifts in the potential suggested the occurrence of fast electron transfers due to the change in the electro-kinetics of the catalyst and the diffusion of hydrazine molecules under the potential gradient. Table 1 summarizes the electrochemical oxidation data of hydrazine oxidation on the basis of the enhancement factor of different systems (individuals and loadings of Ru), contrasted with the significant enhancement factor of hybrid SRu-mC<sub>3</sub>N<sub>4</sub>. This further supports its enhanced activity toward hydrazine oxidation. Detailed calculations are given in Supplementary Information S6 [37].

Moreover, Figure 3C represents the concentration-dependent performance of SRu-mC<sub>3</sub>N<sub>4</sub> in the range from 0  $\mu$ M to 12  $\mu$ M hydrazine, demonstrating a linear correlation between increasing concentration and current density. Furthermore, based on electrocatalytic performance of 4  $\mu$ M hydrazine in 0.5 M KOH solution, this concentration is used for further scan-rate dependent studies, as shown in Figure 3D. Interestingly, with increases in scan rate the current density also increases. The above results of these concentration and scan rate studies confirm that hydrazine oxidation is a diffusion-controlled process for SRu-mC<sub>3</sub>N<sub>4</sub> [38,39].

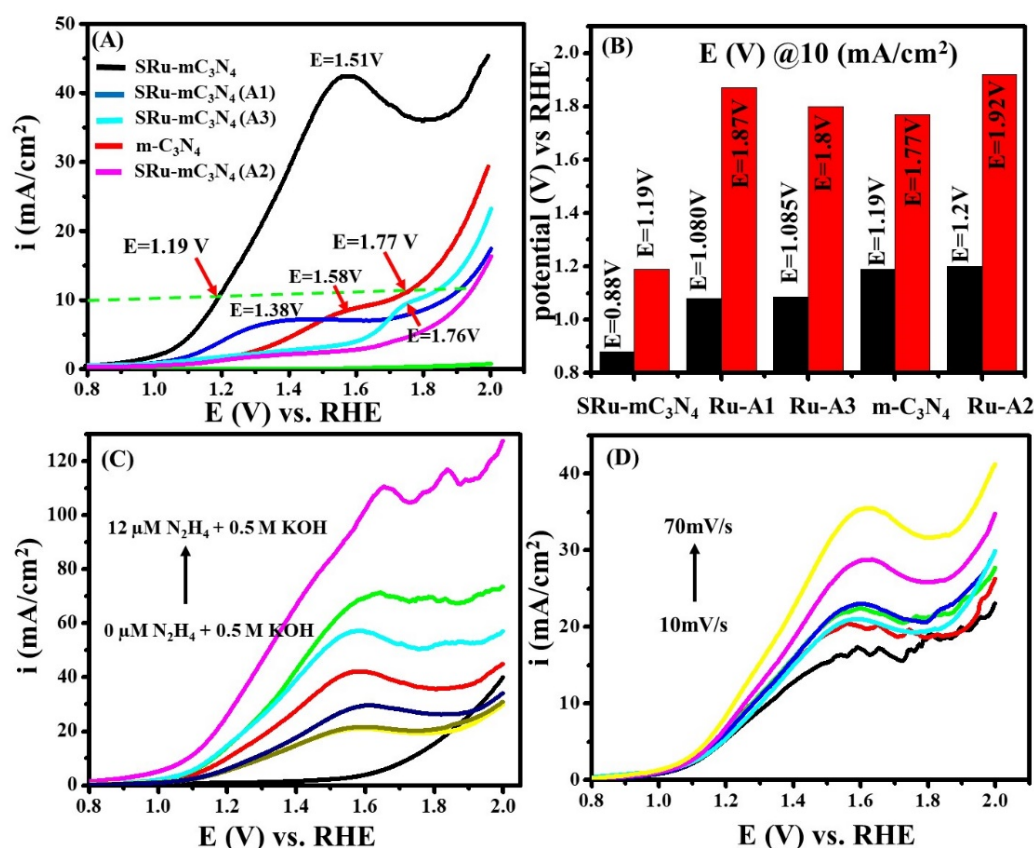


**Figure 3.** (A) Superimposed linear sweep voltammetry (LSV) for the bare GCE (green colour), SRu-mC<sub>3</sub>N<sub>4</sub> (A2), m-C<sub>3</sub>N<sub>4</sub>, SRu-mC<sub>3</sub>N<sub>4</sub> (A3), SRu-mC<sub>3</sub>N<sub>4</sub> (A1), and SRu-mC<sub>3</sub>N<sub>4</sub> in 6 μM N<sub>2</sub>H<sub>4</sub> + 0.5 M KOH at 50 mV/s. (B) Histogram of onset (black bar) oxidation potential and 10 mA/cm<sup>2</sup> (red bar) current density vs. RHE. Superimposed LSV for (C) SRu-mC<sub>3</sub>N<sub>4</sub> for different concentrations (0, 1, 2, 4, 6, 8, 10, 12 μM—black, yellow, dark yellow, blue, red, cyan, green, magenta in colour respectively) of hydrazine in 0.5 M KOH and (D) Scan-rate dependent studies using 4 μM N<sub>2</sub>H<sub>4</sub> in 0.5 M KOH at different scan rates in the range of 10–70 mV/s (black, red, cyan, green, blue, magenta, yellow colours for 10 to 70 mV/s respectively).

**Table 1.** Comparison of different parameters from LSV data for 6 μM N<sub>2</sub>H<sub>4</sub> + 0.5 M KOH at a scan rate of 50 mV/s toward the bare GCE, m-C<sub>3</sub>N<sub>4</sub>, and SRu-mC<sub>3</sub>N<sub>4</sub> for potential at 1.3 V vs. RHE.

Sr. No.	Electrocatalyst	@Potential (V) vs. RHE	Current Density (mA/cm <sup>2</sup> )	Enhancement Factor ( $\eta$ )
(1)	bare GCE	1.3	0.85	-
(2)	m-C <sub>3</sub> N <sub>4</sub>	1.3	3.2	376
(3)	SRu-mC <sub>3</sub> N <sub>4</sub> (A1)	1.3	5.25	617
(4)	SRu-mC <sub>3</sub> N <sub>4</sub> (A3)	1.3	3.28	386
(5)	SRu-mC <sub>3</sub> N <sub>4</sub> (A2)	1.3	3.1	364
(6)	SRu-mC <sub>3</sub> N <sub>4</sub>	1.3	19.2	2258

The enhancement in electro-kinetic parameters was calculated using charge-transfer resistance in EIS studies, with an applied potential for hydrazine oxidation at 1.19 V vs. RHE taken from 10 mA/cm<sup>2</sup>, as shown in Figure 4A. In EIS studies, smaller semicircles ( $R_{ct}$ ) reveal better electron transfer,  $R_{ct}$  is the charge transfer resistance of the oxidation reaction,  $R_s$  is the electrical resistance of the electrolyte, and  $C_{dl}$  is the constant phase element to determine the double-layer capacitance of the WE. Interpretations of the equivalent circuit and their values for SRu-mC<sub>3</sub>N<sub>4</sub> are given in Supplemental Information Figure S4A. Herein, SRu-mC<sub>3</sub>N<sub>4</sub> demonstrates a smaller charge transfer ( $R_{ct}$ -2950  $\Omega$ ), compared with

SRu-mC<sub>3</sub>N<sub>4</sub>(A1) (Rct-5050 Ω), SRu-mC<sub>3</sub>N<sub>4</sub> (A3) (Rct-9990 Ω), and SRu-mC<sub>3</sub>N<sub>4</sub> (A2) (Rct-10030 Ω). This suggests more activity towards the charge transfer potential of hydrazine oxidation at the electrified interface, where mC<sub>3</sub>N<sub>4</sub> shows higher Rct values of 13 Ω and 200 Ω. The bode plot represents the phase angle, with an alternating potential current versus the frequency of the SRu-mC<sub>3</sub>N<sub>4</sub> electrocatalyst. Furthermore, we used EIS data for the calculated bode plot, (see Supplementary Information Figure S4B) which reflects the efficient and fast electron transfer of all the electrocatalysts. The characteristic peak frequency shifts to a lower value indicate efficient electron transfer in the hydrazine oxidation reaction with SRu-mC<sub>3</sub>N<sub>4</sub>. This confirms that SRu-mC<sub>3</sub>N<sub>4</sub> promotes higher activity than other catalysts, possibly due to m-C<sub>3</sub>N<sub>4</sub> serving as a platform for informal electron transfer, with greater surface area and greater chemical stability toward the hydrazine oxidation. The stability studies using chronoamperometric measurements confirm that SRu-mC<sub>3</sub>N<sub>4</sub> has an extremely steady performance: up to 5000 s at an applied potential of 1.3 V vs. RHE, compared with SRu-mC<sub>3</sub>N<sub>4</sub>, SRu-mC<sub>3</sub>N<sub>4</sub> (A1), SRu-mC<sub>3</sub>N<sub>4</sub> (A2), and SRu-mC<sub>3</sub>N<sub>4</sub> (A3). The few irregularities/kinks that can be observed in the black plot line in Figure 4B may be due to the interaction of hydrazine molecules with surface-active Ru sites on SRu-mC<sub>3</sub>N<sub>4</sub>, or due to the further adsorption of by-products, i.e., H<sub>2</sub> and N<sub>2</sub> gaseous molecules. These EIS and chronoamperometric (i-t) measurements confirm an efficient and enhanced activity of SRu-mC<sub>3</sub>N<sub>4</sub> with their synergistic platform, compared with bare mC<sub>3</sub>N<sub>4</sub> toward hydrazine oxidation reactions. Furthermore, we performed experiments with long-term stability tests that have identified real applications in the field of electrocatalysis. The stability test of SRu-mC<sub>3</sub>N<sub>4</sub> was measured in 6 μM N<sub>2</sub>H<sub>4</sub> + 0.5 M KOH at an applied potential of 0.3 V. The results show a minute decomposition rate (6–8%) after 50 h (see Supplementary Information Figure S5). Moreover, the morphology and structure of the SRu-mC<sub>3</sub>N<sub>4</sub> electrocatalyst, recovered after the HzOR studies, were confirmed by the HR-TEM and Raman spectra images (see Supplementary Information Figure S6). Notably, some HR-TEM images confirmed the formation of Ru nanoparticles on the support of mC<sub>3</sub>N<sub>4</sub> (see Supplemental Information Figure S6A–D). Moreover, in the Raman spectra of the recovered SRu-mC<sub>3</sub>N<sub>4</sub> electrocatalyst, the D and G band intensity slightly increased (see Supplementary Information Figure S6E). These proposed studies demonstrate a lower potential for H<sub>2</sub> generation from the oxidation of hydrazine hydrate on SRu-mC<sub>3</sub>N<sub>4</sub>, compared with similar previously studied systems from the literature. These comparisons are summarized in Figure 5 and in Supplementary Information Table S1 [40–48].

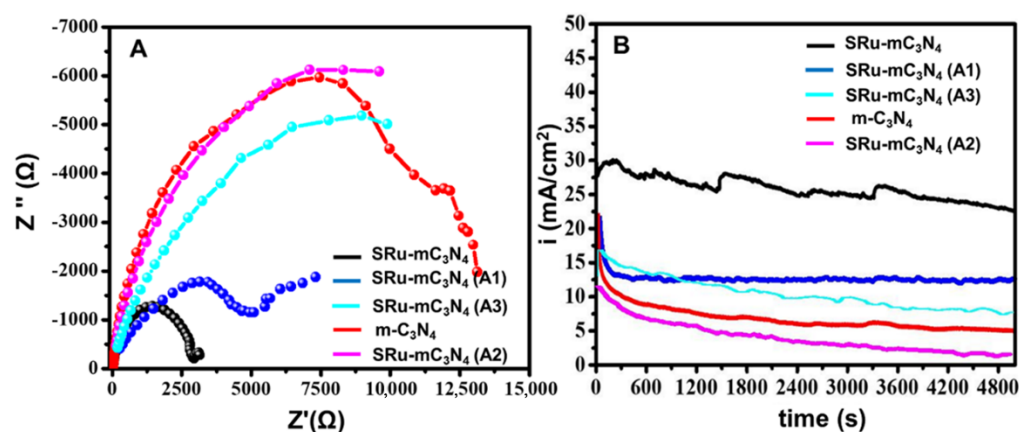


**Figure 4.** (A) Electrochemical impedance spectroscopic (EIS) measurements: SRu-mC<sub>3</sub>N<sub>4</sub> (A2), m-C<sub>3</sub>N<sub>4</sub>, SRu-mC<sub>3</sub>N<sub>4</sub> (A3), SRu-mC<sub>3</sub>N<sub>4</sub> (A1), and SRu-mC<sub>3</sub>N<sub>4</sub> in 6 μM N<sub>2</sub>H<sub>4</sub> + 0.5 M KOH for an AC frequency range of 10–1000 Hz. (B) Chronoamperometric studies of m-C<sub>3</sub>N<sub>4</sub> (I) and SRu-mC<sub>3</sub>N<sub>4</sub> (II) in 6 μM N<sub>2</sub>H<sub>4</sub> + 0.5 M KOH at an applied potential of 1.3 V vs. RHE (based on obtained current density of 20 mA/cm<sup>2</sup>).

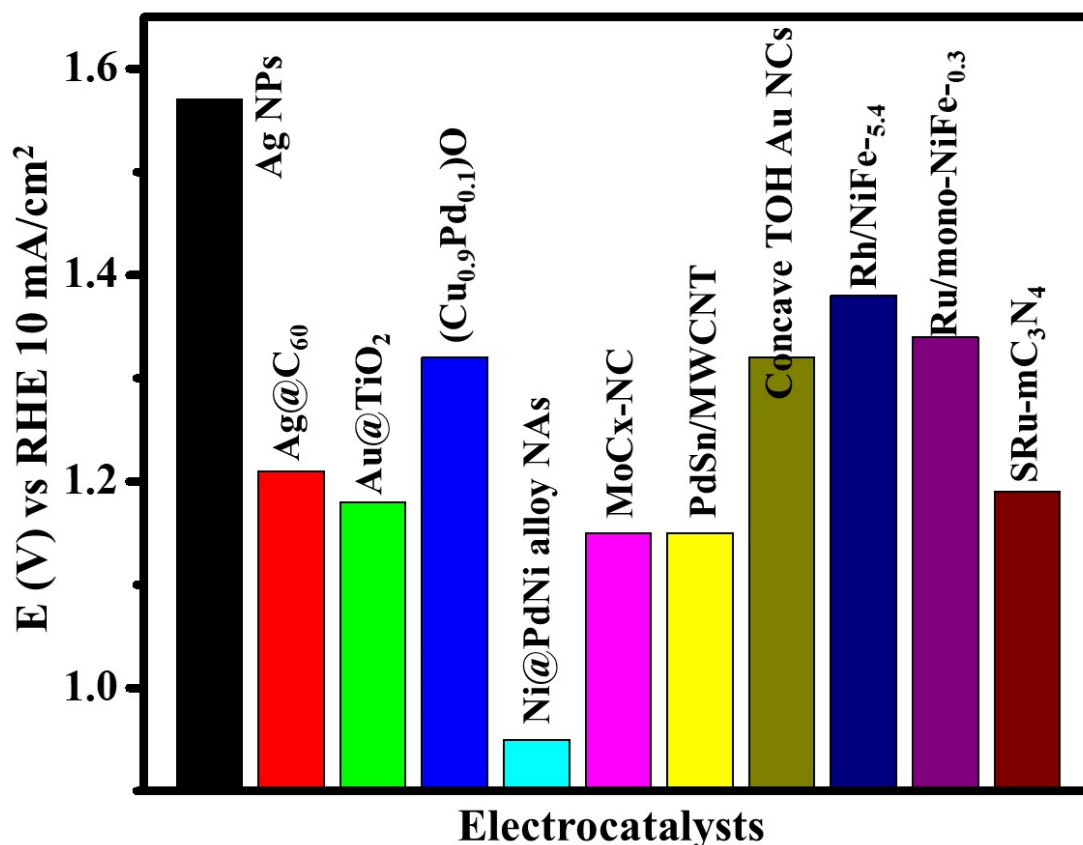


**Figure 5.** Electrochemical performance of hydrazine oxidation in previously reported systems from the literature on hydrazine oxidation reactions.

## 2.2. Mechanistic Pathway for Electrochemical Hydrazine Oxidation on SRu-mC<sub>3</sub>N<sub>4</sub>

Figure 6 demonstrates the typical steps involved in the electrochemical hydrazine oxidation reaction on SRu-mC<sub>3</sub>N<sub>4</sub>, as follows: (4) an efficient adsorption of the hydrazine molecule on the active site of N-Ru-N in the presence of SRu-mC<sub>3</sub>N<sub>4</sub>, (5) electron transfer, where the rate of transfer determines the overall efficiency of the active interface, (6) the three-electron transfer process occurs in a rapid reaction producing dinitrogen (N<sub>2</sub>), as shown below in Equations (4)–(6) [42]:



Previous studies have reported that the decomposition of hydrazine relates to the elongation of the N-H bond, involving four consecutive dehydration steps, such as [19]



Electrochemical data evidences that smooth HzOR occurs on SRu-mC<sub>3</sub>N<sub>4</sub> due to the internal formation of Ru-N/C intercalation in the first coordination shell, attaining synergy in the N-Ru-N connection. This contributes to the synergy between the single Ru atoms and the mC<sub>3</sub>N<sub>4</sub> nanosheets of the SRu-mC<sub>3</sub>N<sub>4</sub> system. However, the mixed valency states of Ru<sup>4+</sup> and Ru<sup>2+</sup> (Figure 1A and Supplementary Information Figure S2) in the presence of the formulated catalyst SRu-mC<sub>3</sub>N<sub>4</sub> are considered to be the reason for enhanced catalytic activity due to apparent charge transfer [49–52].

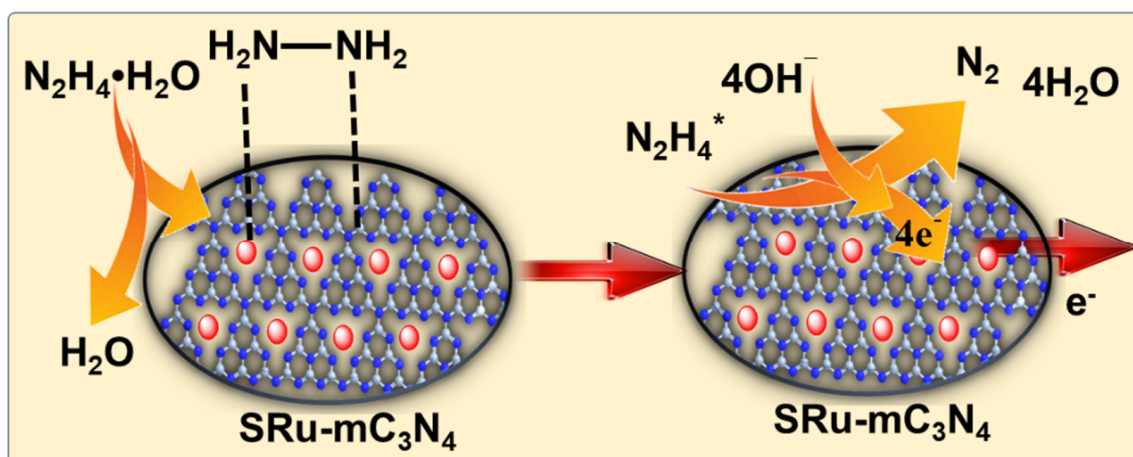


**Figure 6.** Schematic demonstration of steps in electrochemical hydrazine oxidation at SRu-mC<sub>3</sub>N<sub>4</sub> anode interface.

### 3. Methods

#### *Experimental Details and Characterization*

Schematic representation for the preparation of the SRu-mC<sub>3</sub>N<sub>4</sub> catalyst is shown in Supplementary Information, Scheme S1, following the reported procedure in our recent research work [18]. In short, dicyanamide is well stirred with calcined SBA-15 to achieve extended absorption inside each pore of the SBA-15 template (Scheme S1, Step 1), and afterwards calcined (Scheme S1, Step 2), followed by treatment with hydrofluoric acid (HF) to remove silica completely and formulate mesoporous carbon nitride (mC<sub>3</sub>N<sub>4</sub>) (Scheme S1, Step 3). Furthermore, the fabricated mC<sub>3</sub>N<sub>4</sub> is used as a photoactive material for the distribution of single-atom ruthenium. In the prescribed process, an aqueous solution of ruthenium (III) chloride was added dropwise to a Millipore aqueous solution of mesoporous carbon nitride during 30 min of sonication, then heated using a microwave (MW) (LG, Power 1000 Watt; P/No MEZ66853207) run 10–20 times for 2 min each time (Scheme S1 Step 4). The next experiment investigated the change in the w/w% loading of Ru on m-C<sub>3</sub>N<sub>4</sub>. The results showed the following: SRu-mC<sub>3</sub>N<sub>4</sub> (A1), (1.35 wt.%); SRu-mC<sub>3</sub>N<sub>4</sub> (A2) (2.74wt.%); and SRu-mC<sub>3</sub>N<sub>4</sub> (A3) (1.86 wt.%).

### 4. Conclusions

In conclusion, an SRu-mC<sub>3</sub>N<sub>4</sub> single-atom electrocatalyst was carefully synthesized and characterized. Morphological studies using transmission electron microscopy (TEM) confirmed the uniform distribution of Ru single atoms on mesoporous carbon nitride (SRu-mC<sub>3</sub>N<sub>4</sub>). Furthermore, spectroscopic analysis by Raman spectroscopy confirmed the formation of defects due to Ru-N and Ru-O bond formation. XPS spectra confirmed Ru in +2 and +4 oxidation states, and consequently exhibited an increase in hydrazine oxidation activity. Improved nanosheets of mesoporous carbon nitride supported single Ru atoms and provided the appropriate structural porosity to further increase the surface area. This in turn provided larger active sites and further improved the mass transport towards the hydrazine oxidation reactions. These active sites in the presence of Ru-O and Ru-N introduce a significant increase in the electrochemical activity towards hydrazine oxidation reactions. The activity studied using LSV data confirmed that SRu-mC<sub>3</sub>N<sub>4</sub> /GCE attains ultra-low potential at 0.88 V vs. RHE and a high current density of 10 mA/cm<sup>2</sup> at 1.19 V vs. RHE, compared with mC<sub>3</sub>N<sub>4</sub>. EIS and chronoamperometry (i-t) studies indicate smaller charge transfer, and hence more activity and higher currents with potential stability on SRu-mC<sub>3</sub>N<sub>4</sub> toward hydrazine oxidation reactions.

**Supplementary Materials:** The following supporting information can be downloaded at: <https://www.mdpi.com/article/10.3390/catal12121560/s1>, Scheme S1. Schematic representation for protocol depicting formulation of ruthenium single atom over mesoporous  $C_3N_4$  (SRu-m $C_3N_4$ ); Figure S1: Wide-angle XRD pattern of SRu-m $C_3N_4$ ; (a) m $C_3N_4$ ; and (b) SRu-m $C_3N_4$ ; Figure S2: High-resolution XPS spectra of SRu-m $C_3N_4$ : (a) Full scan; (b) N1s spectra of SRu-m $C_3N_4$ ; (c) Ru 3d High-resolution XPS spectra of SRu-m $C_3N_4$  with carbon; Figure S3: Superimposed linear sweep voltammetry (LSV) for the (I) SRu-m $C_3N_4$  in 0.5 M KOH (II) SRu-m $C_3N_4$  in 6  $\mu$ M N $_2$ H $_4$  + 0.5 M KOH at a scan rate of 50 mV/s; Figure S4: (A) (i) equivalent circuit and (ii) their values for SRu-m $C_3N_4$ , (B) Bode plot calculated by using EIS data of different electrocatalysts in 6  $\mu$ M N $_2$ H $_4$  + 0.5 M KOH; Figure S5: Chronoamperometric studies of SRu-m $C_3N_4$  in 6  $\mu$ M N $_2$ H $_4$  + 0.5 M KOH at an applied potential of 1.3 V vs. RHE (based on obtained current density of 20 mA/cm $^2$ ); Figure S6: (A–D) HR-TEM images, and (E) Raman spectra of SRu-m $C_3N_4$  catalyst after electrocatalytic hydrazine oxidation reaction study; Table S1: Electrochemical performance of previously reported HzOR systems from the literature. References [40–48] are cited in Supplementary Materials.

**Author Contributions:** A.M. designed and conducted all experiments, P.S. synthesized and characterized the SRu-m $C_3N_4$  single-atom catalyst. S.K. carried out Raman analysis. R.G.K. helped in characterization. S.D. took over data analysis and editing. H.B.K., J.F. and R.Z. helped in the characterization part and co-wrote the manuscript. B.R.S. and M.B.G. proposed and supervised the whole project, funding acquisition, and assisted in the writing process and data analysis. All authors have read and agreed to the published version of the manuscript.

**Funding:** This research received no external funding.

**Acknowledgments:** The authors gratefully acknowledge the support by the Operational Program Research, Development and Education—European Regional Development Fund (project no. CZ.02.1.01/0.0/0.0/16\_019/0000754) and by the ERDF project “Development of pre-applied research in nanotechnology and biotechnology” (project no. CZ.02.1.01/0.0/0.0/17\_048/0007323) of the Ministry of Education, Youth and Sports of the Czech Republic. R.Z. thanks the Czech Science Foundation for financial support (project no. 19-27454X). A.M. is thankful to MJRF (MS) for fellowship-2021-22/1042 (414). H.B.K. would like to gratefully acknowledge the Institute of Chemical Technology, Mumbai for providing a fellowship for doctoral study.

**Conflicts of Interest:** The authors declare no competing interest.

## References

1. Cai, W.; Yao, Y.-X.; Zhu, G.-L.; Yan, C.; Jiang, L.-L.; He, C.; Huang, J.-Q.; Zhang, Q. A review on energy chemistry of fast-charging anodes. *Chem. Soc. Rev.* **2020**, *49*, 3806–3833. [[CrossRef](#)] [[PubMed](#)]
2. Farmahini, A.H.; Krishnamurthy, S.; Friedrich, D.; Brandani, S.; Sarkisov, L. Performance-Based Screening of Porous Materials for Carbon Capture. *Chem. Rev.* **2021**, *121*, 10666–10741. [[CrossRef](#)] [[PubMed](#)]
3. Bourdrel, T.; Annesi-Maesano, I.; Alahmad, B.; Maesano, C.N.; Bind, M.-A. The impact of outdoor air pollution on COVID-19: A review of evidence from in vitro, animal, and human studies. *Eur. Respir. Rev.* **2021**, *30*, 200242. [[CrossRef](#)] [[PubMed](#)]
4. Tan, X.; Han, L.; Zhang, X.; Zhou, W.; Li, W.; Qian, Y. A review of current air quality indexes and improvements under the multi-contaminant air pollution exposure. *J. Environ. Manag.* **2020**, *279*, 111681. [[CrossRef](#)] [[PubMed](#)]
5. Munde, A.V.; Mulik, B.B.; Chavan, P.P.; Sapner, V.S.; Narwade, S.S.; Mali, S.M.; Sathe, B.R. Electrocatalytic Ethanol Oxidation on Cobalt–Bismuth Nanoparticle-Decorated Reduced Graphene Oxide (Co–Bi@rGO): Reaction Pathway Investigation toward Direct Ethanol Fuel Cells. *J. Phys. Chem. C* **2021**, *125*, 2345–2356. [[CrossRef](#)]
6. Peng, L.; Wei, Z. Catalyst Engineering for Electrochemical Energy Conversion from Water to Water: Water Electrolysis and the Hydrogen Fuel Cell. *Engineering* **2020**, *6*, 653–679. [[CrossRef](#)]
7. Jiao, F.; Xu, B. Electrochemical Ammonia Synthesis and Ammonia Fuel Cells. *Adv. Mater.* **2018**, *31*, e1805173. [[CrossRef](#)]
8. Kowalik, P.; Antoniak-Jurak, K.; Blesznowski, M.; Herrera, C.; Larrubia, M.; Alemany, L.J.; Pieta, I.S. Biofuel steam reforming catalyst for fuel cell application. *Catal. Today* **2015**, *254*, 129–134. [[CrossRef](#)]
9. Khalafallah, D.; Zhi, M.; Hong, Z. Development Trends on Nickel-Based Electrocatalysts for Direct Hydrazine Fuel Cells. *ChemCatChem* **2020**, *13*, 81–110. [[CrossRef](#)]
10. Rosca, V.; Duca, M.; de Groot, M.T.; Koper, M.T.M. Nitrogen Cycle Electrocatalysis. *Chem. Rev.* **2009**, *109*, 2209–2244. [[CrossRef](#)]
11. Munde, A.V.; Mulik, B.B.; Dighole, R.P.; Sathe, B.R. Urea Electro-Oxidation Catalyzed by an Efficient and Highly Stable Ni–Bi Bimetallic Nanoparticles. *ACS Appl. Energy Mater.* **2021**, *4*, 13172–13182. [[CrossRef](#)]
12. Kadam, R.G.; Zhang, T.; Zoralová, D.; Medve, M.; Bakandritsos, A.; Tomanec, O.; Petr, M.; Chen, J.Z.; Miller, J.T.; Otyepka, M.; et al. Single Co-Atoms as Electrocatalysts for Efficient Hydrazine Oxidation Reaction. *Small* **2021**, *17*, e2006477. [[CrossRef](#)]

13. Carvalho, L.L.; Colmati, F.; Tanaka, A.A. Nickel–palladium electrocatalysts for methanol, ethanol, and glycerol oxidation reactions. *Int. J. Hydrogen Energy* **2017**, *42*, 16118–16126. [[CrossRef](#)]
14. Yang, G.-W.; Gao, G.-Y.; Wang, C.; Xu, C.-L.; Li, H.-L. Controllable deposition of Ag nanoparticles on carbon nanotubes as a catalyst for hydrazine oxidation. *Carbon* **2008**, *46*, 747–752. [[CrossRef](#)]
15. Du, J.; Xiang, D.; Zhou, K.; Wang, L.; Yu, J.; Xia, H.; Zhao, L.; Liu, H.; Zhou, W. Electrochemical Hydrogen Production Coupled with Oxygen Evolution, Organic Synthesis, and Waste Reforming. *Nano Energy* **2022**, *104*, 107875. [[CrossRef](#)]
16. Sun, H.; Kim, H.; Song, S.; Jung, W. Copper foam-derived electrodes as efficient electrocatalysts for conventional and hybrid water electrolysis. *Mater. Rep. Energy* **2022**, *2*, 100092. [[CrossRef](#)]
17. Sun, H.; Xu, X.; Kim, H.; Jung, W.; Zhou, W.; Shao, Z. Electrochemical Water Splitting: Bridging the Gaps between Fundamental Research and Industrial Applications. *Energy Environ. Mater.* **2022**, e12441. [[CrossRef](#)]
18. Sharma, P.; Kumar, S.; Tomanec, O.; Petr, M.; Chen, J.Z.; Miller, J.T.; Varma, R.S.; Gawande, M.B.; Zbořil, R. Carbon Nitride-Based Ruthenium Single Atom Photocatalyst for CO<sub>2</sub> Reduction to Methanol. *Small* **2021**, *17*, 2006478. [[CrossRef](#)]
19. Zhao, Y.; Jia, N.; Wu, X.-R.; Li, F.-M.; Chen, P.; Jin, P.-J.; Yin, S.; Chen, Y. Rhodium Phosphide Ultrathin Nanosheets for Hydrazine Oxidation Boosted Electrochemical Water Splitting. *Appl. Catal. B Environ.* **2020**, *270*, 118880. [[CrossRef](#)]
20. Liu, X.; He, J.; Zhao, S.; Liu, Y.; Zhao, Z.; Luo, J.; Hu, G.; Sun, X.; Ding, Y. Self-Powered H<sub>2</sub> Production with Bifunctional Hydrazine as Sole Consumable. *Nat. Commun.* **2018**, *9*, 4365. [[CrossRef](#)]
21. Ojha, K.; Farber, E.M.; Burshtein, T.Y.; Eisenberg, D. A Multi-Doped Electrocatalyst for Efficient Hydrazine Oxidation. *Angew. Chem. Int. Ed.* **2018**, *57*, 17168–17172. [[CrossRef](#)]
22. Narwade, S.S.; Mali, S.M.; Tanwade, P.D.; Chavan, P.P.; Munde, A.V.; Sathe, B.R. Highly Efficient Metal-Free Ethylenediamine-Functionalized Fullerene (EDA@C 60) Electrocatalytic System for Enhanced Hydrogen Generation from Hydrazine Hydrate. *New J. Chem.* **2022**, *46*, 14004–14009. [[CrossRef](#)]
23. Muthukumar, P.; John, S.A. Synergistic effect of gold nanoparticles and amine functionalized cobalt porphyrin on electrochemical oxidation of hydrazine. *New J. Chem.* **2014**, *38*, 3473–3479. [[CrossRef](#)]
24. Wang, H.; Ding, J.; Kannan, P.; Ji, S. Cobalt nanoparticles intercalated nitrogen-doped mesoporous carbon nanosheet network as potential catalyst for electro-oxidation of hydrazine. *Int. J. Hydrogen Energy* **2020**, *45*, 19344–19356. [[CrossRef](#)]
25. Ding, J.; Kannan, P.; Wang, P.; Ji, S.; Wang, H.; Liu, Q.; Gai, H.; Liu, F.; Wang, R. Synthesis of nitrogen-doped MnO/carbon network as an advanced catalyst for direct hydrazine fuel cells. *J. Power Sources* **2018**, *413*, 209–215. [[CrossRef](#)]
26. Gawande, M.B.; Fornasiero, P.; Zbořil, R. Carbon-Based Single-Atom Catalysts for Advanced Applications. *ACS Catal.* **2020**, *10*, 2231–2259. [[CrossRef](#)]
27. Pieta, I.S.; Kadam, R.G.; Pieta, P.; Mrdenovic, D.; Nowakowski, R.; Bakandritsos, A.; Tomanec, O.; Petr, M.; Otyepka, M.; Kostecki, R.; et al. The Hallmarks of Copper Single Atom Catalysts in Direct Alcohol Fuel Cells and Electrochemical CO<sub>2</sub> Fixation. *Adv. Mater. Interfaces* **2021**, *8*, 2001822. [[CrossRef](#)]
28. Niu, W.; Yang, Y. Graphitic Carbon Nitride for Electrochemical Energy Conversion and Storage. *ACS Energy Lett.* **2018**, *3*, 2796–2815. [[CrossRef](#)]
29. Wang, Y.; Li, Z.; Jin, Z.; Xing, W.; Zhuang, Z.; Ye, J.; Wei, X.; Cao, R.; Gu, L.; Sun, S.; et al. Single-Atom Rh/N-Doped Carbon Electrocatalyst for Formic Acid Oxidation. *Nat. Nanotechnol.* **2020**, *15*, 390–397. [[CrossRef](#)]
30. Mulik, B.B.; Munde, A.V.; Bankar, B.D.; Biradar, A.V.; Sathe, B.R. Highly Efficient Manganese Oxide Decorated Graphitic Carbon Nitride Electrocatalyst for Reduction of CO<sub>2</sub> to Formate. *Catal. Today* **2020**, *370*, 104–113. [[CrossRef](#)]
31. Wen, J.; Xie, J.; Chen, X.; Li, X. Applied Surface Science A Review on G-C<sub>3</sub>N<sub>4</sub> -Based Photocatalysts. *New J. Chem.* **2017**, *391*, 72–123. [[CrossRef](#)]
32. Mulik, B.B.; Bankar, B.D.; Munde, A.V.; Chavan, P.P.; Biradar, A.V.; Sathe, B.R. Electrocatalytic and Catalytic CO<sub>2</sub> Hydrogenation on ZnO/g-C<sub>3</sub>N<sub>4</sub> Hybrid Nanoelectrodes. *Appl. Surf. Sci.* **2021**, *538*, 148120. [[CrossRef](#)]
33. Kumar, S.; Gawande, M.B.; Kopp, J.; Kment, S.; Varma, R.S.; Zbořil, R. P- and F-co-doped Carbon Nitride Nanocatalysts for Photocatalytic CO<sub>2</sub> Reduction and Thermocatalytic Furanics Synthesis from Sugars. *ChemSusChem* **2020**, *13*, 5231–5238. [[CrossRef](#)] [[PubMed](#)]
34. Aghajani, H.; Tabrizi, A.T.; Ghorbani, R.; Behrangi, S.; Stupavska, M.; Abdian, N. Evaluation of Electrochemical Hydrogen Storage Capability of Three-Dimensional Nano-Structured Nitrogen-Doped Graphene. *J. Alloy. Compd.* **2022**, *906*, 164284. [[CrossRef](#)]
35. Yousefi Bonab, S.S.; Kouzehgar, H.; Taghizadeh Tabrizi, A.; Aghajani, H. Assessment of the Effect of Electrophoretic Deposition Parameters on Hydrogen Storage Performance of Graphene Oxide Layer Applied on Nickel Foam. *Int. J. Hydrogen Energy* **2022**, *47*, 2491–2499. [[CrossRef](#)]
36. Ghorbani, R.; Behrangi, S.; Aghajani, H.; Taghizadeh Tabrizi, A.; Abdian, N. Application of Synthesized Porous 3D Graphene Structure for Electrochemical Hydrogen Storage. *Mater. Sci. Eng. B* **2021**, *268*, 115139. [[CrossRef](#)]
37. Munde, A.V.; Mulik, B.B.; Dighole, R.P.; Sathe, B.R. Cobalt Oxide Nanoparticle-Decorated Reduced Graphene Oxide (Co<sub>3</sub>O<sub>4</sub>-RGO): Active and Sustainable Nanoelectrodes for Water Oxidation Reaction. *New J. Chem.* **2020**, *44*, 15776–15784. [[CrossRef](#)]
38. Munde, A.V.; Mulik, B.B.; Chavan, P.P.; Sathe, B.R. Enhanced Electrocatalytic Activity towards Urea Oxidation on Ni Nanoparticle Decorated Graphene Oxide Nanocomposite. *Electrochim. Acta* **2020**, *349*, 136386. [[CrossRef](#)]
39. Miao, R.; Compton, R.G. Mechanism of Hydrazine Oxidation at Palladium Electrodes: Long-Lived Radical Di-Cation Formation. *Electrochim. Acta* **2021**, *388*, 138655. [[CrossRef](#)]

40. Narwade, S.S.; Mulik, B.B.; Mali, S.M.; Sathe, B.R. Silver Nanoparticles Sensitized C60(Ag@C60) as Efficient Electrocatalysts for Hydrazine Oxidation: Implication for Hydrogen Generation Reaction. *Appl. Surf. Sci.* **2017**, *396*, 939–944. [[CrossRef](#)]
41. Roy, N.; Bhunia, K.; Terashima, C.; Fujishima, A.; Pradhan, D. Citrate-Capped Hybrid Au-TiO<sub>2</sub> Nanomaterial for Facile and Enhanced Electrochemical Hydrazine Oxidation. *ACS Omega* **2017**, *2*, 1215–1221. [[CrossRef](#)] [[PubMed](#)]
42. Zhang, X.; Shi, S.; Yin, H. CuPd Alloy Oxide Nanobelts as Electrocatalyst Towards Hydrazine Oxidation. *ChemElectroChem* **2019**, *6*, 1514–1519. [[CrossRef](#)]
43. Du, M.; Sun, H.; Li, J.; Ye, X.; Yue, F.; Yang, J.; Liu, Y.; Guo, F. Integrative Ni@Pd-Ni Alloy Nanowire Array Electrocatalysts Boost Hydrazine Oxidation Kinetics. *ChemElectroChem* **2019**, *6*, 5581–5587. [[CrossRef](#)]
44. Deng, J.; Li, X.; Imhanria, S.; Chen, K.; Deng, X.; Wang, W. Molybdenum Carbide-Nitrogen Doped Carbon Composites as Effective Non-Precious Electrocatalyst for Direct Hydrazine Fuel Cell. *Electrochim. Acta* **2021**, *384*, 138417. [[CrossRef](#)]
45. Er, O.F.; Cavak, A.; Aldemir, A.; Kivrak, H. Hydrazine Electrooxidation Activities of Novel Carbon Nanotube Supported Tin Modified Palladium Nanocatalysts. *Surf. Interfaces* **2022**, *28*, 101680. [[CrossRef](#)]
46. Liu, F.; Jiang, X.; Wang, H.-H.; Chen, C.; Yang, Y.-H.; Sheng, T.; Wei, Y.-S.; Zhao, X.-S.; Wei, L. Boosting Electrocatalytic Hydrazine Oxidation Reaction on High-Index Faceted Au Concave Trioctahedral Nanocrystals. *ACS Sustain. Chem. Eng.* **2022**, *10*, 696–702. [[CrossRef](#)]
47. Liu, G.; Wang, Z.; Shen, T.; Zheng, X.; Zhao, Y.; Song, Y.-F. Atomically Dispersed Rh-Doped NiFe Layered Double Hydroxides: Precise Location of Rh and Promoting Hydrazine Electrooxidation Properties. *Nanoscale* **2021**, *13*, 1869–1874. [[CrossRef](#)]
48. Wang, Z.; Xu, S.-M.; Xu, Y.; Tan, L.; Wang, X.; Zhao, Y.; Duan, H.; Song, Y.-F. Single Ru Atoms with Precise Coordination on a Monolayer Layered Double Hydroxide for Efficient Electrooxidation Catalysis. *Chem. Sci.* **2019**, *10*, 378–384. [[CrossRef](#)]
49. Gao, Y.; Xue, Y.; He, F.; Li, Y. Controlled Growth of a High Selectivity Interface for Seawater Electrolysis. *Proc. Natl. Acad. Sci. USA* **2022**, *119*, e2206946119. [[CrossRef](#)]
50. Zheng, X.; Xue, Y.; Zhang, C.; Li, Y. Controlled Growth of Multidimensional Interface for High-Selectivity Ammonia Production. *CCS Chem.* **2022**, 1–10. [[CrossRef](#)]
51. Gao, Y.; Xue, Y.; Qi, L.; Xing, C.; Zheng, X.; He, F.; Li, Y. Rhodium Nanocrystals on Porous Graphdiyne for Electrocatalytic Hydrogen Evolution from Saline Water. *Nat. Commun.* **2022**, *13*, 5227. [[CrossRef](#)] [[PubMed](#)]
52. Xue, Y.; Huang, B.; Yi, Y.; Guo, Y.; Zuo, Z.; Li, Y.; Jia, Z.; Liu, H.; Li, Y. Anchoring Zero Valence Single Atoms of Nickel and Iron on Graphdiyne for Hydrogen Evolution. *Nat. Commun.* **2018**, *9*, 1460. [[CrossRef](#)] [[PubMed](#)]